High-Energy 2-μm Doppler Lidar for Wind Measurements

Grady J. Koch*[a], Jeffrey Y. Beyon[b] , Bruce W. Barnes[a], Mulugeta Petros[c], Jirong Yu[a] , Farzin Amzajerdian[a], Michael J. Kavaya[a], and Upendra N. Singh[a]

[a]NASA Langley Research Center, MS 468, Hampton, VA USA 23681
[b]California State University, Dept. of Electrical and Computer Engineering, Los Angeles, CA USA
[c]Science and Technology Corporation, 10 Basil Sawyer Drive, Hampton, VA USA 23666

*e-mail: grady.j.koch@nasa.gov, voice: 757-864-3850, fax: 757-864-8828

ABSTRACT

High-energy 2-μm wavelength lasers have been incorporated in a prototype coherent Doppler lidar to test component technologies and explore applications for remote sensing of the atmosphere. Design of the lidar is presented including aspects in the laser transmitter, receiver, photodetector, and signal processing. Calibration tests and sample atmospheric data are presented on wind and aerosol profiling.

1. INTRODUCTION

Recent advances in high-energy 2-μm solid-state laser technology have enabled lidar applications for long range wind sensing. Wind profiling with 2-μm lidar has already shown merit using low-energy (1-10 mJ) laser transmitters based on thulium.[1,2,3] And the addition of stronger energy lasers promises to boost the applicability of the coherent Doppler technique to farther distances and higher altitudes. Comparable or higher pulse energy that the coherent Doppler lidar described here has been demonstrated but at wavelengths of 1-μm from a neodymium laser and 10-μm from CO_2 lasers.[4,5,6,7] The 2-μm based approach overcomes a disadvantage with the 1-μm lidar in that the 2-μm wavelength offers a much higher level of eye safety. The 2-μm wavelength laser is appealing over the 10-μm laser because the 2-μm laser is a solid-state medium of more convenient and robust implementation than CO_2 gas. A further advantage of the lidar described here is the demonstrated capability of adding amplification stages to the laser for even more pulse energy that might be required for a spaceborne lidar.[8] Research at NASA is developing lidar technology for satellite-based observation of wind on a global scale. The ability to profile tropospheric wind is a key measurement for understanding and predicting atmospheric dynamics and is a critical measurement for improving weather forecasting and climate modeling.[9] Homeland security applications have been proposed to provide wind data for accurate transport prediction of a plume release of a nuclear, biological, or chemical agent.[10]

We report here on technology developments and lidar system demonstrations aimed at long-range wind applications. A new laser composition of Ho:Tm:LuLiF is used that optimizes output energy. The coherent heterodyne receiver is also discussed, including advances with an integrated photodiode/preamp in a dual-balanced configuration. A lidar system testbed has been built from

these components and integrated with a real-time signal processing and display computer. This testbed has been named VALIDAR from the concept of "validation lidar," in that it can serve as a component technology calibration and validation source for future airborne and spaceborne lidar missions. VALIDAR is housed within a mobile trailer for field measurements.

2. LIDAR DESIGN

The optical layout of VALIDAR is shown in Figure 1 and a list of specifications is given in Table 1. Transmitter and receiver subsystems are each described separately, with the transmitter considered to consist of the pulsed laser, continuous wave (CW) laser, and the optics associated with coupling the two. The receiver is considered to be the transmit/receive switch, telescope, and photodetector. Not shown in Figure 1 is a scanner mounted through the roof of the trailer for steering the lidar beam.

2.1. Laser Transmitter

The 2-μm wavelength is advantageous in a coherent Doppler lidar for several reasons. First, it offers a high level of eye safety with a maximum permissible exposure of 100 mJ/cm^2.[11] Second, the 2-μm wavelength is strongly backscattered by aerosols in the atmosphere, from which the Doppler shift indicates wind speed. Third, holmium solid-state lasers can produce a high level of pulse energy at 2.05 μm.

A holmium laser material, with an activator of thulium, is used to generate the 2-μm wavelength. The holmium/thulium composition has traditionally been used with host materials of yttrium aluminum garnet (YAG) and yttrium lithium fluoride (YLiF), and Henderson et. al used a flashlamp-pumped Ho:Tm:YAG laser in a Doppler lidar.[12] The transmitter described here uses a host material of lutetium lithium fluoride (LuLiF) pumped by diode laser arrays. LuLiF allows more output energy than YAG or YLiF, while retaining high damage tolerance and a low level of thermal lensing.[13] An experiment in which YLiF and LuLiF crystals of the same holmium and thulium concentrations were interchanged with the same diode pumping showed 20% more pulse energy from the LuLiF crystal. The transmitter described here is of a single laser oscillator, but considerable work has gone into oscillator-amplifier designs showing as much as 1-J of energy per pulse.[8] Other work has shown a laser oscillator that is conductively cooled, eliminating the water cooling of the pulsed laser described here.[14]

As diagrammed in Figure 2, the Ho:Tm:LuLiF rod is contained in a pump head using conductively cooled laser diode arrays. Water cooling is used for the heat sink of the diode arrays, but the laser diodes are not directly cooled with water. Six AlGaAs diode arrays side pump the laser rod; each array has six bars that can provide up to 600 mJ near 792 nm in a 1-ms pulse. Three sets of two diode arrays, side by side, are arranged 120^{o} apart around the laser rod circumference. The laser rod has a diameter of 4 mm and is encased in a 6-mm outer-diameter fused-silica glass tube for water cooling of the laser rod; the coolant temperature is kept at 15 C. The 20-mm long laser rod is doped with 6% Tm and 0.4% Ho. The resonator is in a ring configuration with a total length of 2.0 m, with an acousto-optic Q-switch to spoil the laser cavity.

A continuous wave (CW) Ho:Tm:YLF laser serves as both an injection seed source and a local oscillator. This laser was originally built by Coherent Technologies, Inc. for the Space

Readiness Coherent Lidar Experiment (SPARCLE).[15] Approximately 10 mW of this CW laser is split off and focused into a polarization maintaining optical fiber for the local oscillator channel. Two channels of heterodyne detection are used: one for that atmospheric backscatter and one for monitoring the outgoing laser pulse. To feed these two channels the local oscillator is split with a fiber optic evanescent wave coupler. The heterodyne pulse monitor is required to create a reference in time (from which to base range calculation) and frequency (from which to base Doppler shift calculation). Taking the pulse monitor from the atmospheric backscatter channel was evaluated in hope of using only one heterodyne detector and reducing the parts count. However, it was found that the gain required on the atmospheric channel photodetector was too high for the pulse monitor, creating a saturated and distorted pulse monitor. The time and frequency references from the distorted monitor were often erroneous, creating time and frequency bias in the output data products. We concluded that two photodetector channels are required with different gain settings.

The rest of the CW energy is used for injection seeding after being frequency shifted 105 MHz by an acousto-optic modulator (AOM). Such an offset sets an intermediate frequency between the local oscillator and pulsed laser output. A series of three Faraday isolators are used between the CW laser and the pulsed laser in order to prevent damage to the CW laser from a counter-propagating laser pulse and to isolate the local oscillator channel from influences by the laser pulse and AOM. If continuously left on, the AOM was found to generate residual amplitude modulation and electromagnetic at its modulation frequency that interfered with the Doppler signals. Hence, the AOM is shut off after the injection seeding takes hold and the laser pulse is formed. The 0^{th} order, non-shifted beam through the AOM is not used in the scheme diagrammed in Figure 1. However, a configuration has been successfully tested to use the 0^{th} order beam coming through the AOM, with the AOM switched off after seeding, as the local oscillator. With

the AOM shut off all of the CW energy input to the AOM is available. This scheme may be beneficial in designs where the CW master oscillator power is limited.

To ensure a single-frequency pulsed output by the injection seeding process, the pulsed laser cavity is actively matched to the frequency of the injection seed by a ramp-and-fire technique.[16] A piezo-electric translator (PZT) mounted to a mirror of the pulsed laser is ramped by voltage, as shown in Figure 3. An InGaAs photodiode circuit views the resonance of the injection seed with the pulsed laser cavity, and resonance peaks occur when the pulsed laser cavity length matches the injection seed frequency. A circuit senses the resonance and fires the Q-switch when this cavity matching condition is determined. This results in a single-frequency output spectrum from the pulsed laser. Successful seeding can be determined by a smooth shape to the laser pulse, as shown in Figure 4, and an approximate doubling of output power as the ring resonator is forced to run in a single direction. The frequency difference between the output pulse and local oscillator, while nominally at 105 MHz, jitters on a shot-to-shot basis by as much as several MHz. Statistics on frequency jitter are presented in Section 2.4.

The Ho:Tm:LuLiF output wavelength can be tuned between 2050 to 2057 nm with the exact wavelength selected by the injection seed. The gain peaks around 2053.5 nm which allows for the easiest injection seeding. Another factor in selecting wavelength is the presence of CO_2 and H_2O lines within the laser's tuning range. Consulting with the HITRAN atmospheric database to avoid these lines and find minimal absorption led us to select the operating wavelength at 2053.47 nm, corresponding to a two-way atmospheric transmission from the ground to 8 km altitude of 87.2%.[17] The presence of these absorption lines can also be exploited to measure gas concentration, with CO_2 being of particular interest. A design very similar to the lidar system described here has been reported for making CO_2 differential absorption lidar measurements.[18]

2.2. Receiver

The basic design of the receiver is similar to those described in use with lower energy 2-μm system.[2,12] Differences with the design used here are in optical fiber rather than free-space routing of optical signals and an improvement in the photodetector implementation using a dual-balanced configuration. The use of optical fiber allows for a convenient and flexible implementation of the devices in the optical path, such that they can be easily disconnected for replacement, diagnostics, or trouble shooting.

The pulsed laser output is transmitted to the atmosphere via a 6-inch diameter off-axis paraboloid telescope. After expansion by the telescope, the output laser beam can be pointed or scanned by a scanner mounted through the roof of the trailer. The outgoing pulse and atmospheric backscatter are separated by a polarization relationship imposed by the combination of a quarter-wave plate and polarizing beam splitter.

Heterodyne detection is provided by InGaAs photodiodes in a dual-balanced configuration as diagrammed in Figure 5. Such a detector configuration has been thoroughly investigated for use in telecommunications applications, but not well known for use in Doppler lidar.[19] The dual-balanced design is used here as it allows collection of all of the atmospheric backscatter and local oscillator through a 50/50 evanescent wave coupler. A more typical design would be to use a single photodiode with a coupler taking 90% of the atmospheric backscatter and 10% of the local oscillator. The dual-balanced configuration has an additional benefit of canceling amplitude noise that may occur in the local oscillator. A photodetector circuit is being used that combines the

photodiodes and amplifiers (in die form) integrated together in the same microelectronic package. Such packaging reduces parasitic capacitance, thus improving performance where a wide bandwidth is needed. A factor of 2.2 reduction in parasitic capacitance has been shown over a previous design using discrete components integrated on a printed circuit board. The circuit used in VALIDAR has a 200 MHz bandwidth, but circuits have been developed with 2 GHz bandwidth.[20]

2.3. Data acquisition and signal processing

Processing of the lidar data is accomplished in real-time with the system diagrammed in Figure 6. Real-time reduction of the heterodyne signal to wind and backscatter data products was taken to be an important feature in order to accommodate future missions, such as from an aircraft with the lidar operating autonomously, in which the transmission or storage of raw data might not be possible.

The heterodyne signal is conditioned by an analog front end that includes an anti-aliasing filter and two different level of amplification switched in to bring the outgoing scatter pulse and atmospheric return within the dynamic range of a digitizer. Sampling by the digitizer is at 500 Ms/s and 8 bit resolution. An example of a single digitized heterodyne signal is shown in Figure 7 in time domain.

Digitized data flows to an array of SHARC digital signal processors (DSP) for real-time reduction of the heterodyne signal to wind and power data products. The DSP, digitizer, and control software are hosted by a single computer over a PCI backplane. Control software includes a program in which the user can set such parameters as number of sample points, number of pulses to

be averaged, scanner angles, and display preferences. An outline of the processing steps for an acquisition along a single line of sight is given in the following:

Step (A): acquire

An individual pulse is digitized starting from a trigger generated by a monitor photodetector. A user-specified number of samples is taken and separated into range bins with a typical setup being 50,000 samples (corresponding to 15 km range) broken into 512 sample bins (corresponding to 153.6 m). The first range bin, however, can be of a longer length of 1024 samples to isolate the outgoing pulse scattered from the lidar optics. The scatter pulse is also called a monitor pulse because it is used to monitor for frequency jitter that may occur in the injection seeding process. Range bin information is converted to range in meters. A number of pulses is acquired for averaging as specified by the user. As an option range bins may to overlapped to smooth the wind measurements in range. For example, the atmospheric measurements shown later were made with range bins overlapped by 50% to provide a data point every 76.8 m.

Step (B): FFT

The power spectrum of the data for each range bin is calculated by a fast Fourier transform (FFT). A Hamming window may be applied as an option.

Step (C): monitor frequency determination

The frequency corresponding to the peak of the spectrum is estimated in the first range bin containing the monitor pulse. This estimated frequency is compared to a user-specified frequency range to check if the laser pulse was properly injection seeded. An unseeded pulse, which occurs for less than 1% of the laser pulses, will have a maximum frequency estimate at a frequency corresponding to the free spectral range of the pulsed laser cavity since multiple modes are beating. Such a mode beating frequency is well away from the intermediate frequency and is easily filtered by this step. If a bad pulse is detected it is discarded from the set so that it will not be included in averaging.

Step (D): shift spectra

Taking the first pulse in the accumulation as the reference, provided it passed the test of the above step, the spectra of the following pulses' atmospheric returns are shifted in frequency to remove the effects of pulse-to-pulse frequency jitter. The amount of shifting applied to each pulse is determined from Step (C).

Step (E): averaging

The jitter-corrected spectra for each range bin are averaged among all the pulses acquired. A typical configuration is to use 20 pulses for averaging.

Step (F): Doppler shift and power estimation

The frequency corresponding to the peak of the spectrum is determined for each range bin and subtracted from the zero Doppler reference frequency. This result is used to determine the Doppler shift. The power spectrum for each range bin is estimated by a periodogram from a 512 point FFT, and the peak value is used for power estimation. With a 512 point FFT at a 500 Ms/s sampling rate, the frequency resolution is just under 1 MHz.

This resolution could be improved by increasing the number of points in the FFT, such as by zero padding. A study of the effects of zero padding showed improvement in wind measurement results if the 512 real samples were padded to a length of 4096 (or more) samples.[21] It was further found, however, that this level of zero padding is not amenable to real-time processing of the wind data products when processing ranges to 15 km. Several other techniques were evaluated to improve range/velocity resolution or improve performance in weak signal regimes in an attempt to bring in more good wind measurements at longer ranges. These techniques have included noise whitening, various windowing functions, and nonparametric spectral estimation.[22,23] The most effective technique found was an adaptive filtering algorithm, that is compatible with real-time implementation.[24] The atmospheric data in Section 3 were generated in real-time using the relatively simple algorithm outlined in described in steps A through G without zero padding or

refined spectral estimation techniques. Future work includes implementing algorithms for optimized resolution and weak SNR conditions that can run in real time.

Each of the above steps may be repeated in different scanner viewing angles. A typical measurement scenario is to steer the laser beam in three directions—two orthogonal azimuths for finding the horizontal wind field and zenith viewing for finding vertical wind motion. Data can be archived either as raw digitized samples or processed Doppler shift and power measurements. The real-time processing system also serves as a post-processor by reading in archived raw data. For more extensive studies of processing algorithms, a more flexible version of the processor has been implemented in LabVIEW. Once a new algorithm has been developed it can be translated into the C+ language for the real-time processor.

2.4 System Performance Testing

A diagnostic test was made of the lidar to verify operation of the combined optical and signal processing systems, with emphasis on verifying a lack of bias in measuring range and speed. The lidar beam was aligned to strike a hard target (a cell phone tower) at 2.8-km range to check that the hard target read at a consistent range and at a consistent zero velocity. While range errors are not typically problematic, velocity errors can occur from the frequency jitter residual from the ramp-and-fire injection seeding. Figure 8a is a histogram of the frequency offset between the local oscillator and transmitted pulse for 6000 consecutive pulses. While nominally set for 105 MHz this

sample set shows that the actual intermediate frequencies were spread from 103 MHz to 112 MHz. With the Doppler shift at 2-μm wavelength being 1 MHz per m/s of wind speed, this large range of frequency jitter must be corrected to obtain accurate wind measurements. The approach for this correction is to measure the jitter on a pulse-to-pulse basis and compensate for the frequency jitter before spectral averaging, as described in Section 2.3.

The efficacy of the frequency jitter compensation is tested in the backscatter from the hard target to verify that the lidar measures the speed at 0 m/s. Figure 8b shows the velocity measured for the same pulse set of Figure 8a. In this experiment the lidar beam was attenuated to an output of less than 1 mJ so that the reflection from the hard target was not saturated. The atmospheric backscatter before the pulse hit the hard target is hence very weak. Though weak, wind measurements were still made from the aerosol backscatter, but the measurements are mostly out of the narrow velocity span set in the data display. Such a narrow span was used to resolve any potential small speed measurements around 0 m/s where the hard target is expected to be. The velocity from the cell phone tower was indeed found consistently at 0 m/s, at least as processed with the velocity resolution from the processing parameters used here and described in Section 2.3. The range measurements to the hard target are also consistent across the measurement set and accurate to within the processor's range resolution of 150-m long range bins.

Further system testing was made by making a side-by-side comparison of VALIDAR with a low-energy commercial Doppler lidar.[25] Statistical comparison of the parallel line-of-sight measurements showed a root-mean-square difference in wind speed measurements of 0.42 m/s.

3. ATMOSPHERIC MEASUREMENTS

3.1 Vertical Wind Profiling

Profiles of the vertical component of wind are shown in Figures 9 and 10. In these data sets the lidar is pointed toward zenith and wind data is continuously sampled over many minutes with 20 pulses grouped together for averaging and processing. Hence, a vertical wind profile is made every 4 s, resulting in 900 wind profiles in Figure 9 and 300 wind profiles in Figure 10. The upper plot in each figure is the wind speed versus altitude and the lower plot is signal power versus altitude. Ordinarily the vertical component of wind is featureless, typically showing speed at or near 0 m/s. The cases of Figures 9 and 10 are unusual in that strong vertical motions occur. Figure 9 was recorded over one hour on the gusty afternoon of April 28, 2005. The signal power shows a typically strong return from the aerosol-rich atmospheric boundary layer (ABL) up to an altitude of approximately 2 km. Above the ABL the aerosol backscatter drops by more than an order of magnitude (a backscatter difference as large as two orders of magnitude between the ABL and free troposphere has been observed in other data). Aerosol backscatter extends to 7.5 to 8.5 km altitude before the signal drops into noise. The maximum altitude of operation with aerosol backscatter is highly variable, with season of the year being a strong factor. Over intermittent operations located at Hampton, Virginia dating back to April 2003 (though with of varying laser pulse energy and lidar designs as development progressed) the minimum altitude of operation was found to occur in late Fall and the maximum altitude was found in late Spring. The lowest and highest maximum altitudes observed were 2 km and 11.5 km, respectively. This qualitative analysis pertains to aerosol backscatter only; clouds may limit range at low altitudes or provide for higher altitude operation from cirrus.

The vertical wind plot shows turbulent motion within the atmospheric boundary layer, but near-zero speed in the free troposphere. Some of the turbulent structure in the boundary layer is seen to be organized in what are perhaps horizontal convective rolls. The wind speed shows updrafts and downdrafts, both peaking at 3 m/s, as the roll advects across the view of the lidar. Above these horizontal rolls a series of buoyancy waves were observed with peak speeds of 2 m/s. A similar measurement scenario has been used to characterize thermals in which birds were observed to be soaring.[26]

Another interesting example of vertical wind structure is shown in Figure 10, taken during a thunderstorm. Various cloud layers are seen in this data, with the early phase of the storm dominated by a low, dense cloud at 1300 m altitude. Under this cloud a sustained updraft reaching 6 m/s occurs as the storm is building up. This updraft subsided and was followed by the low cloud layer breaking up. Rain is seen near the middle of the data set, marked by speeds reaching 12 m/s. This downward speed is believed to be the fall of the rain by gravity enhanced by downdraft pushing the rain drops. Liquid water is effective at absorbing the lidar's energy, and the signal power plot shows a variation in the maximum range as the rate of precipitation varies. Water was also pooling on the output window of the scanner, and the anomaly at 13:44 results from intentionally spinning the scanner to remove the pooled water. The intense rain from this storm quickly dissipated to a relatively calm atmosphere, as seen in the lack of turbulence in the wind speed after 13:45.

3.2 Horizontal and Vertical Wind Profiling

A horizontal wind profile can be measured by viewing two orthogonal azimuths at the same elevation, determining speed along each azimuth, and vector summing the components as a function of altitude. In this approach the vertical wind component is assumed to be zero. The data acquisition and control software, described in Section 2, automates steering of the scanner and collection of data. A typical measurement scenario is to view three different angles with 20 pulses averaged at each angle. In the following data the horizontal wind field was measured with the beam oriented at 45 degree elevation (Section 3.2.1 and 3.2.3) or 3 degree elevation (Section 3.2.2) at azimuths facing north and east, the third angle used is set toward zenith for the vertical wind record. Scanner angles are calibrated to true compass directions by steering the lidar beam onto a hard target at a location known in relation to the scanner output by GPS survey. At 5 Hz pulse repetition rate such a three-direction measurement set requires 25-35 seconds to complete depending on the extent of data archiving selected. This measurement set, which provides horizontal and vertical wind profiles, can then be automatically repeated.

3.2.1 High Altitude Wind Profiling

A sample of such a measurement is shown in Figure 11 recorded on June 28, 2005 over a span of 7 ½ hours, with a frontal system passing through in the middle of the data set. The horizontal wind speed within the boundary layer significantly increased with the passage of the front, with the speed peaking in a jet formation of 16 m/s. A higher altitude jet is also seen forming in the later part of the data. Before passage of the front the horizontal wind speed shows a transition at 4400 m altitude, above which the speed increased by 3-5 m/s. By referring to the

zenith-viewing signal power measurement in the lowest plot this transition at 4400 m altitude also corresponds to a change in aerosol density.

The wind direction before the front passage shows a shift in direction between the atmospheric boundary layer and free troposphere, a commonly observed phenomenon, shifting in this case from southerly to south-westerly flow at higher altitudes. The frontal system brings a reversal of this relationship of south-westerly flow in the boundary layer and southerly flow in the free troposphere.

The lower two plots are the wind speed and backscatter power from the third scanner position of the lidar beam looking toward zenith. The signal power shows clouds below 1000 m and above 6500 m before the front. The low cloud layer lifted with the front. Near 18:30 rain developed, showing up as enhanced backscatter and also appearing in the velocity measurement as downward motion reaching 4 m/s. An interesting feature of the rain is that the downward motion ceases at an altitude near the transition from the atmospheric boundary layer and the free troposphere, suggesting that the rain evaporates. The lack of rain observed at ground level also indicates that the precipitation was in the form of virga.

In a separate study, a new algorithm has been applied to the data of Figure 11 that improves the performance of wind measurements in weak SNR conditions.[24] This refined algorithm was run, however, in post processing as opposed to the real-time results shown in Figure 11.

3.2.2 Low Altitude Wind Profiling

In order to probe the lower atmosphere with higher spatial resolution the elevation angle of the scanner can be decreased. For example, Figure 12 shows a wind profile taken with an elevation

angle of 3 degrees elevation to compose the horizontal wind. The vertical measurements are on a different scale, and since the lidar is blind for the first 300 m of range the horizontal and vertical wind measurements do not correspond well in altitude. That is, the low elevation angle for the horizontal wind measurements is set to probe the lower atmosphere while the zenith-looking vertical measurement is suited to higher altitudes. The trigonometry of the horizontal measurement must also be kept in mind when interpreting the wind data, in that the horizontal distance from the lidar at which the measurements at altitude are made can be large. For example, the horizontal distance from the lidar at which the 500-m altitude measurement is made is 9.5 km.

An interesting observation of this low attitude measurement example is the movement of gusts, which can be seen as slanted features in the wind speed measurements of Figure 12. An ambient wind of 1-3 m/s exists with the occurrence of gusts of 4.5 m/s. The wind speed measurements show that the 4.5 m/s gusts are first detected at higher altitudes then lower altitudes. This phenomenon is attributed to the low elevation angle of the lidar beam. That is, if a gust uniform with altitude approached the lidar it would appear first at high altitudes and slide to lower altitudes. By this reasoning the speed of the gust could also be calculated by translating altitude to horizontal distance and noting the time over which the altitude dropped. But making such a calculation using the slope of the features in Figure 12 results in a gust speed of 3.2 m/s, slower than the speed extracted directly from Doppler shift. This indirect slope-based calculation, though, assumes that the gust is a uniform vertically standing plane when it may actually be sloped, an eddy, or of disorganized spatial structure. This configuration of lidar scan demonstrates an ability to provide a warning of oncoming gusts.

3.2.3 Cirrus Cloud

High altitude cirrus clouds have also been characterized with the lidar as shown in Figure 13. The cloud was observed on December 16, 2005, a time of year when jet stream winds can occur over the geographical area in which the lidar is located (Hampton, Virginia). A continuum of wind speeds occurred in altitudes from 7 km to 10 km ranging from 40 m/s to 65 m/s, and showing the highest known wind speed to be measured with a coherent Doppler lidar. A similarly continuous variation was found in the wind direction varying through 20 degrees. The zenith viewing measurements show a downward motion within the cloud, presumably ice crystal virga, ranging from 1 m/s to 3 m/s with lower speeds more prevalent at the bottom of the cloud. The cloud descended in height over the 3-hour data set, and the backscatter measurement reveals the cloud to be dissipating.

4. CONCLUSION

A lidar has been developed from a new type of laser material (Ho:Tm:LuLiF), capable of generating high-energy 2-μm wavelength pulses for wind and aerosol measurements. Atmospheric testing has shown the ability to measure wind to higher altitudes than the lower-energy mm lasers now in use. The system design is scalable to a future space-based instrument, and the atmospheric tests of the lidar described here were used to predict performance of a space-based lidar.[27] More pulse energy that the 100-mJ class instrument described here can be achieved by adding amplification stages to the output of the pulsed laser oscillator, an approach that has been taken to demonstrate an output energy of 1-J per pulse. Moving toward a spaceborne instrument also

requires hardening the lidar design for vibration, autonomy, and extreme environments. Work is currently underway toward a ruggedized version capable of operation from an aircraft. The atmospheric wind measurements described have proved this testbed to be a valuable tool, as a ground-based instrument, for performing atmospheric research.

The receiver design is similar to that of Doppler lidars used in previous research, but with the addition of a dual-balanced photodetector that improves the efficiency of both the receiver and the use of local oscillator power. A data processing system has been built capable of real-time reduction of the heterodyne signal to wind and signal backscatter power measurements to ranges of 15 km.

ACKNOWLEGEMENTS

This work was supported by the NASA Laser Risk Reduction Program and the Integrated Program Office.

REFERENCES

1. S.M. Hannon, S.W. Henderson, J.A. Thomson, and P. Gatt, “Autonomous lidar wind field sensor: performance predictions,” SPIE Volume 2832, pp. 76-91 (1996).

2. C.J. Grund, R.M. Banta, J.L. George, J.N. Howell, M.J. Post, R.A. Richter, A.M. Weickmann, “High-Resolution Doppler Lidar for Boundary Layer and Cloud Research,” J. Atmos. And Ocean. Tech, 18, 376-393 (2001).
3. P. Brockman, B.C. Barker, G.J. Koch, D.P.C. Nguyen, and C.L. Britt, “Coherent pulsed lidar sensing of wake vortex position and strength, winds and turbulence in airport terminal areas,” *Tenth Biennial Coherent Laser Radar Technologies and Applications Conference*, pp. 12-15 (1999).
4. J.G. Hawley, R. Targ, S.W. Henderson, C.P. Hale, M.J. Kavaya, and D. Moerder, “Coherent launch-site atmospheric wind sounder: theory and experiment,” Appl. Opt. 32, 4557-4568 (1993).
5. R.T. Menzies and R.M. Hardesty, “Coherent Doppler lidar for measurement of wind fields,” Proc. IEEE **77**, 449-462 (1989).
6. M.J. Post and R.E. Cupp, “Optimizing a pulsed Doppler lidar,” Appl. Opt. **29**, 4145-4158 (1990).
7. Ch. Werner, P.H. Flamant, O. Reitebuch, F. Kopp, J. Streicher, S. Rahm, E. Nagel, M. Klier, H. Herrmann, C. Loth, P. Delville, Ph. Drobinski, B. Romand, Ch. Boitel, D. Oh, J. Lopez, M. Meissonier, D. Bruneau, and A. Dabas, “Wind infrared Doppler lidar instrument,” Opt. Eng. **40**, 115-125 (2001).
8. J. Yu, B.C. Trieu, E.A. Modlin, U.N. Singh, M.J. Kavaya, S. Chen, Y. Bai, P.J. Petzar, and M. Petros, “1 J/pulse Q-switched 2 μm solid state laser,” Opt. Lett. **31** 462-464 (2006).
9. W. Baker, G.D. Emmitt, F. Robertson, R. Atlas, J. Molinari, D. Bowdle, J. Paergle, R.M. Hardesty, R. Menzies, T. Krishnamurti, R. Brown, M.J. Post, J. Anderson, A. Lorenc, and J.

McElroy, “Lidar-Measured Winds from Space: A Key Component for Weather and Climate Prediction,” Bull. Amer. Meteor. Soc. **76**, 869-888 (1995).

10. R.J. Fleming, “National environmental observing system to mitigate the effects of a nuclear-biological-chemical (NBC) attacks: strategic and tactical,” SPIE Volume 5071, pp. 22-32 (2003).
11. American National Standard Z136.6-2005, “Safe use of lasers outdoors.”
12. S.W. Henderson, C.P. Hale, J.R. Magee, M.J. Kavaya, and A.V. Huffaker, “Eye-safe coherent laser radar system at 2.1 μm using Tm,Ho:YAG lasers,” Opt. Lett. **16**, 773-775 (1991).
13. B.M. Walsh, N.P. Barnes, M. Petros, J. Yu, and U.N. Singh, “Spectroscopy and modeling of solid state lanthanide lasers: Application to trivalent Tm^{3+} and Ho^{3+} in $YLiF_4$ and $LuLiF_4$,” J. Appl. Phys. 95, 3255-3271 (2004).
14. M. Petros, J. Yu, T. Melak, B. Trieu, S. Chen, U. Singh, and Y. Bai, “High energy totally conductive cooled, diode pumped, 2 μm laser,” Advanced Solid-State Photonics Conference, OSA Trends in Optics and Photonics Volume ? , 2005.
15. C. Hale, S.W. Henderson, and D.M. D’Epagnier, “Tunable Highly-Stable Maser/Local Oscillator Lasers for Coherent Lidar Applications,” in *Proceedings of the Tenth Biennial Coherent Laser Radar Technology and Applications Conference*, 115-118, 1999.
16. S.W. Henderson, E.Y. Yuen, and E.S. Fry, “Fast resonance detection technique for single-frequency operation of injection seeded Nd:YAG lasers,” Opt. Lett. **11**, 715-717 (1986).
17. USF HITRAN-PC, Version 2.51 (Ontar Corporation, North Andover, Mass., 1996)

18. G.J. Koch, B.W. Barnes, M. Petros, J.Y. Beyon, F. Amzajerdian, J. Yu, R.E. Davis, S. Ismail, S. Vay, M.J. Kavaya, and U.N. Singh, "Coherent Differential Absorption Lidar Measurement of CO_2," Appl. Opt. **43**, 5092-5099 (2004).
19. M. Cvijetic, "Coherent and Nonlinear Lightwave Communications," Artech house, Inc., Norwood, MA (1996).
20. F. Amzajerdian, "Analysis of Optimum Heterodyne Receivers for Coherent Lidar Applications," Proc. of 21th International Laser Radar Conference, Quebec, Canada, July 8-12, 2002.
21. J.Y. Beyon and G.J. Koch, "Resolution study of wind parameter estimates by a coherent Doppler lidar system," Proc. of SPIE Vol.6214, 621403 (2006).
22. J.Y. Beyon, G.J. Koch, and Z. Li, "Noise normalization and windowing functions for VALIDAR in wind parameter estimation," Proc. of SPIE Vol.6214, 621404 (2006).
23. J.Y. Beyon and G.J. Koch, "Wind profiling by a coherent Doppler lidar system VALIDAR with a subspace decomposition approach," Proc. of SPIE Vol.6236, 623605-1 (2006).
24. J. Y. Beyon and G. J. Koch, "Novel Nonlinear Adaptive Doppler Shift Estimation Technique for the Coherent Doppler Validation Lidar" Opt. Eng. accepted for publication, August 2006.
25. G.D. Emmitt, S.A. Wood, and G.J. Koch, "Comparison of VALIDAR and GWOLF Doppler Lidar Measurements," 2nd Symposium on Lidar Atmospheric Applications, American Meteorological Society 85th Annual Meeting, 2005.
26. G.J. Koch, "Using a Doppler light detection and ranging (lidar) system to characterize an atmospheric thermal providing lift for Soaring Raptors," J. Field Ornithol. 77 (2006),

27. M.J. Kavaya, G.J. Koch, F. Amzajerdian, B.W. Barnes, R.E. Davis, U.N. Singh, R.G. Frehlich, “Estimating Space Performance of a Coherent Doppler Wind Lidar by Inverting Ground Performance,” Working Group on Space-Based Lidar Winds, Welches, OR, July 2005.
28. A.E. Siegman, “Defining, measuring, and optimizing laser beam quality,” Proc. SPIE 1868 (1993).

Laser material:	Ho:Tm:LuLiF
Pulse energy:	90 mJ operationally, capable of 100 mJ
Pulse width:	140 ns
Pulse repetition rate:	5 Hz, 10 Hz at reduced energy
Spectrum:	single frequency
Wavelength:	2053.5 nm
Wavelength tuning:	3-4 nm including CO_2 lines
Beam quality (M^2):	< 1.2 times diffraction limit[28]
Detector:	InGaAs in dual-balanced configuration
Telescope aperture:	6 inches
Scanner:	8.5 inch aperture full hemispherical coverage

Table 1: Specifications of VALIDAR

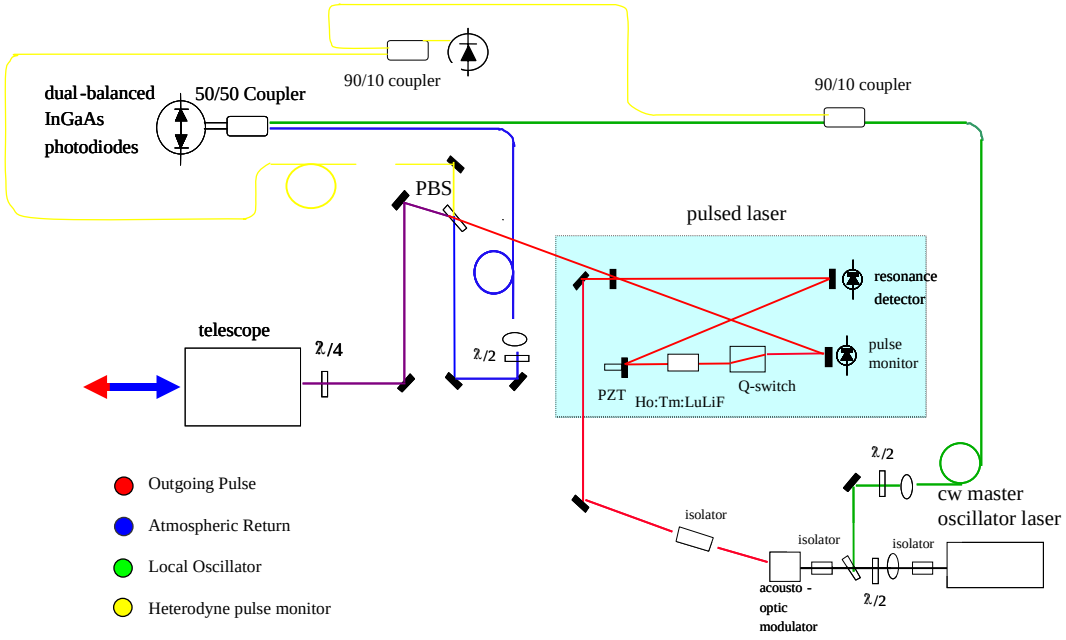

Figure 1: Optical layout of VALIDAR. Fiber optic paths are indicated by a circular bend in the path.

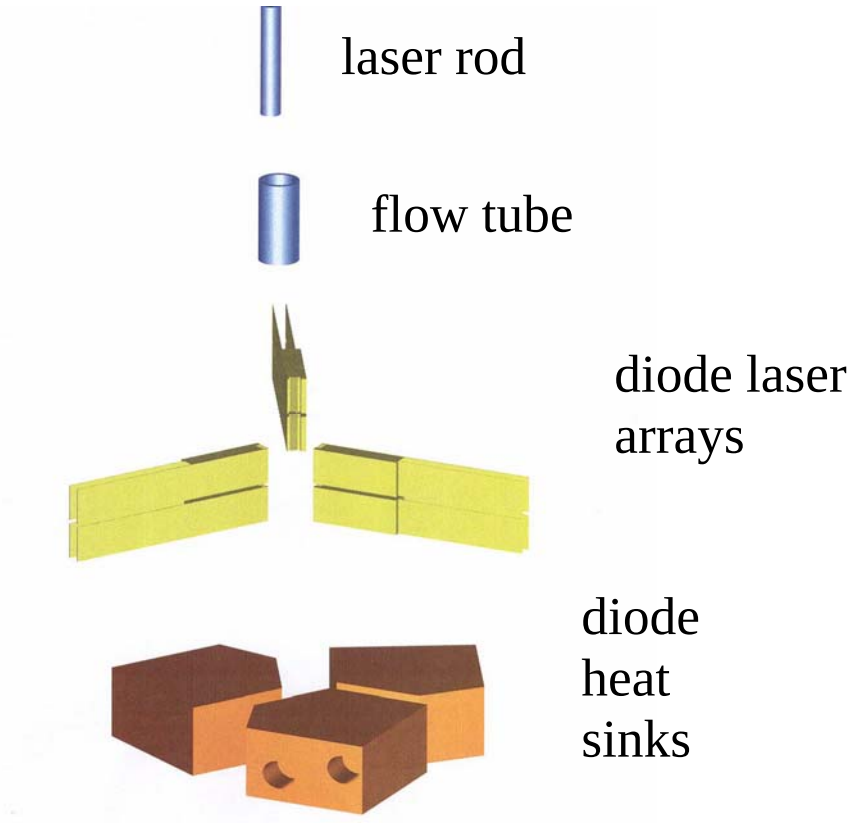

Figure 2: Exploded view of laser head assembly.

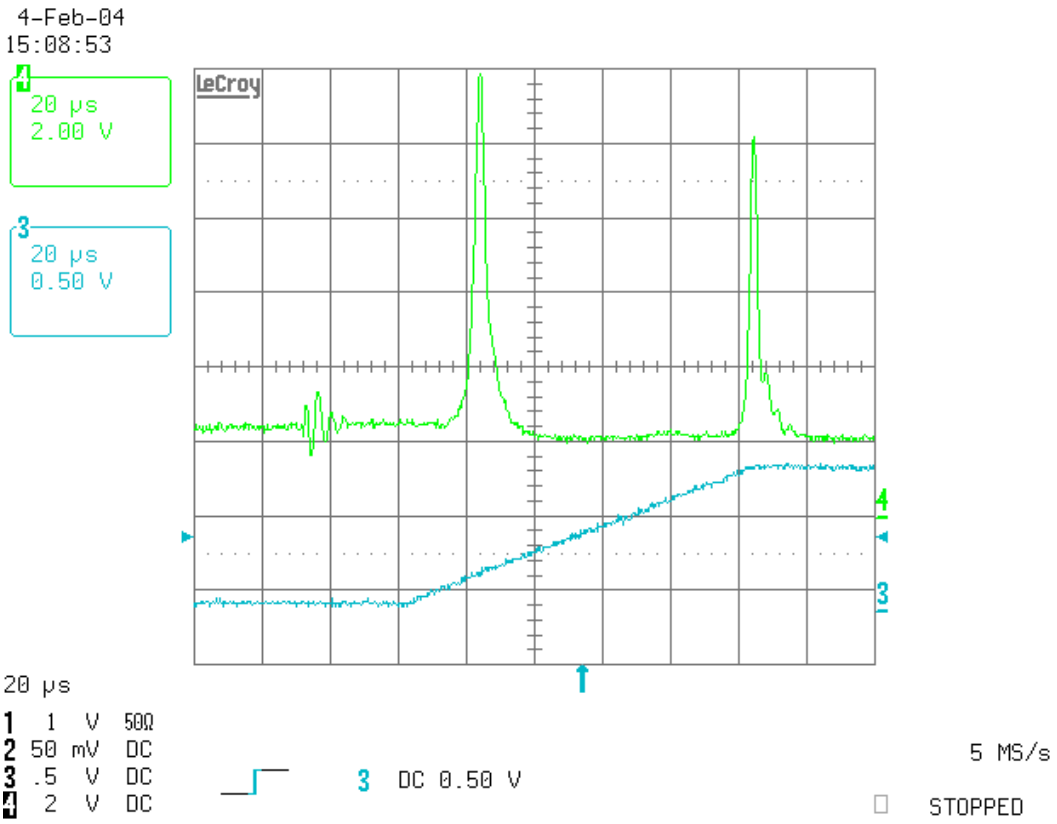

Figure 3: Signal involved with ramp-and-fire injection seeding technique. The lower curve is a monitor of the ramp voltage applied to the piezo-electric translator (PZT) to change the pulsed laser cavity length. The upper plot shows the CW injection seed in resonance with the pulsed laser cavity. An electronic circuit fires the Q-switch when a resonance is detected.

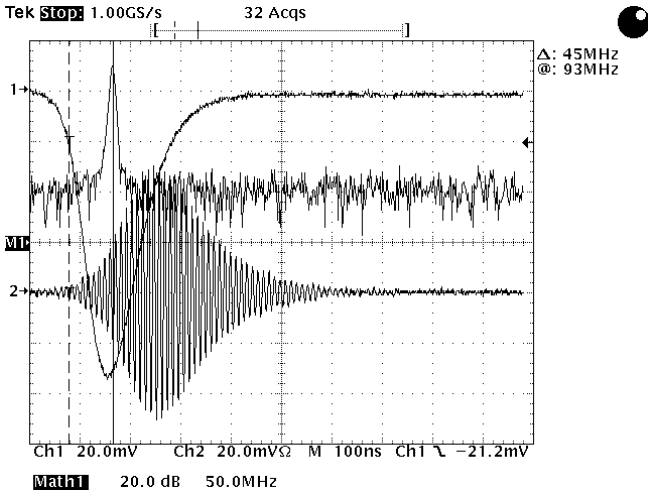

Figure 4: Injection seeding results in a single frequency spectrum as monitored by a photodiode outside the laser cavity. The temporal profile (channel 1) of the pulse shows a pulse width of 142 ns and a smooth gaussian shape. Without injection seeding this gaussian envelope would be modulated by mode beating between longitudinal modes of the laser cavity. Channel 2 and its discrete Fourier transform (middle plot) show the heterodyne signal of the laser pulse—this signal is used by the signal processing system to determine pulse-to-pulse frequency jitter.

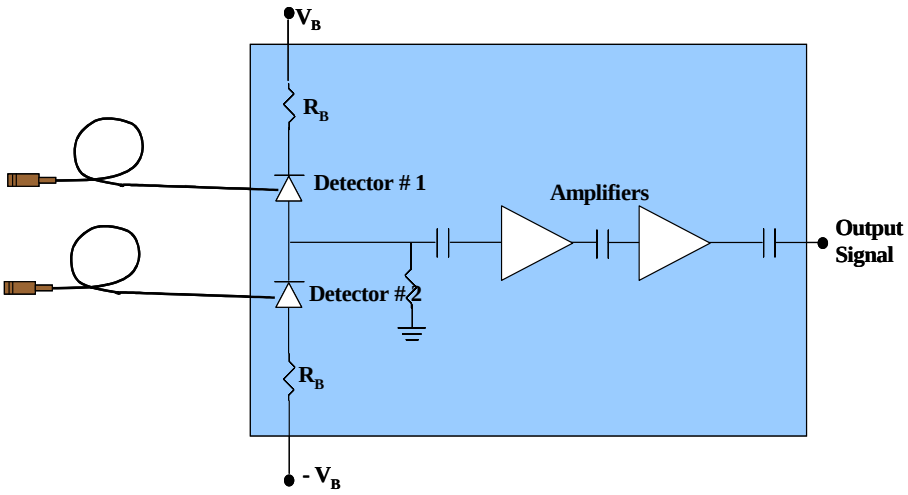

Figure 5: Diagram of the dual-balanced heterodyne detector. The polarity of the photodiodes allows cancellation of AM noise that might be present on the local oscillator. Fiber optic pigtails are attached to the photodiodes.

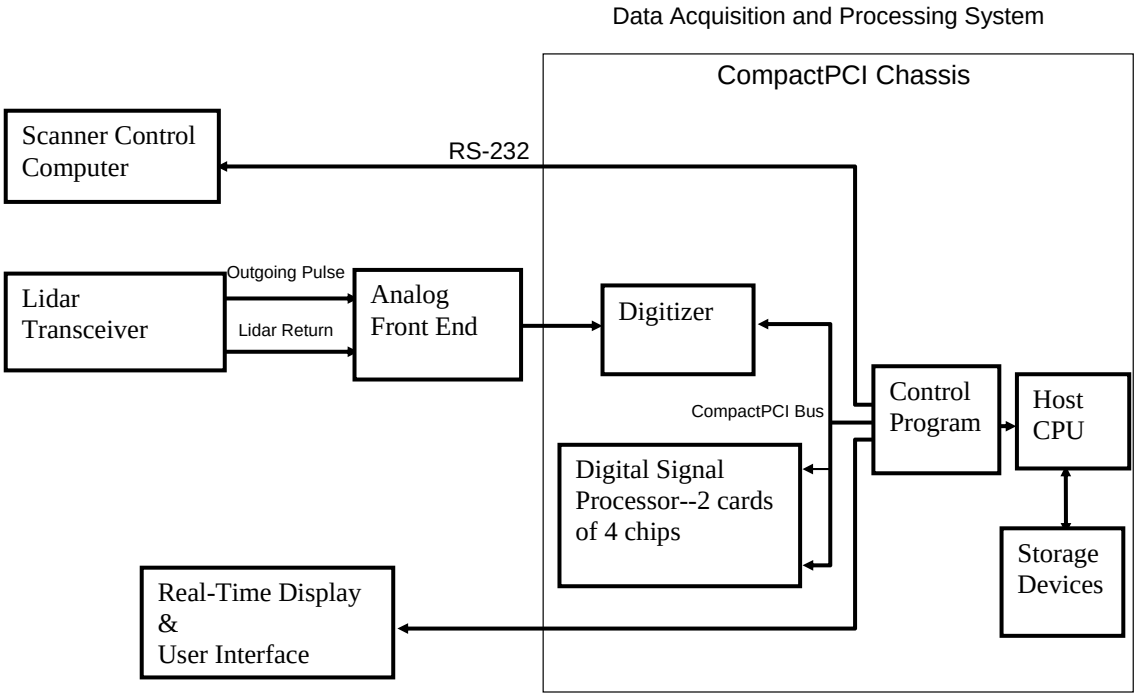

Figure 6: Layout of the VALIDAR electronics and signal processing system.

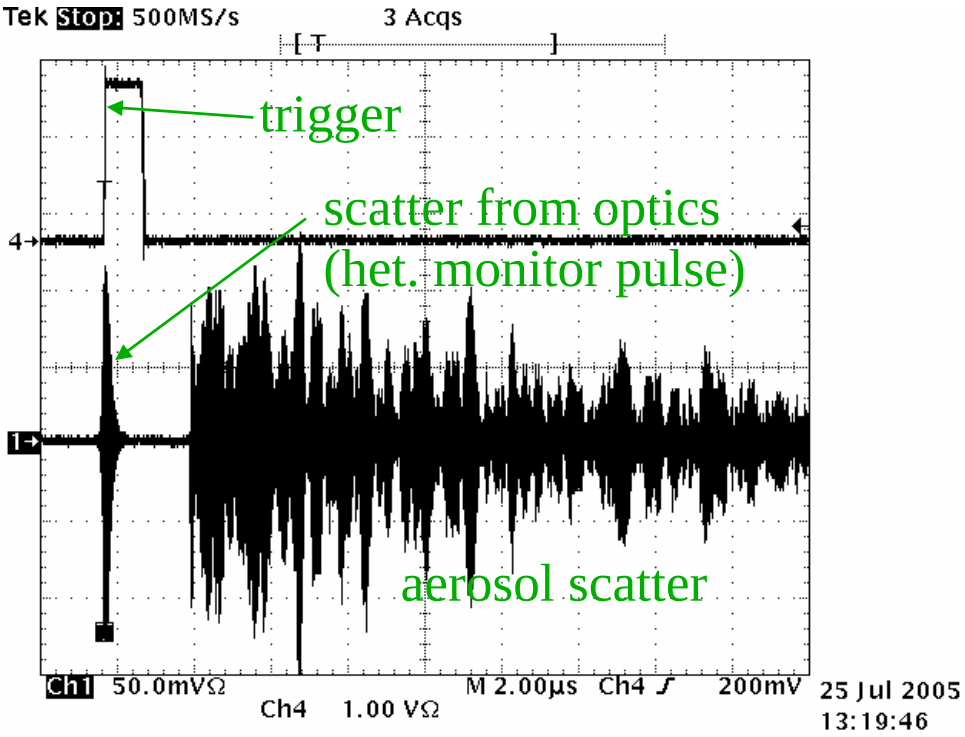

Figure 7: Backscatter (lower plot) from a single pulse. Two heterodyne detectors are used to compose this signal with a switch selecting the two channels—the transient from this electronic switch can by seen at approximately 1.2 µs from the trigger. Before the switch is the pulse monitor from which the zero frequency for Doppler processing is determined. The second channel is taken from the dual-balanced detector for the atmospheric backscatter. $1/R^2$ decay in the signal strength can be seen in the envelope of the backscatter.

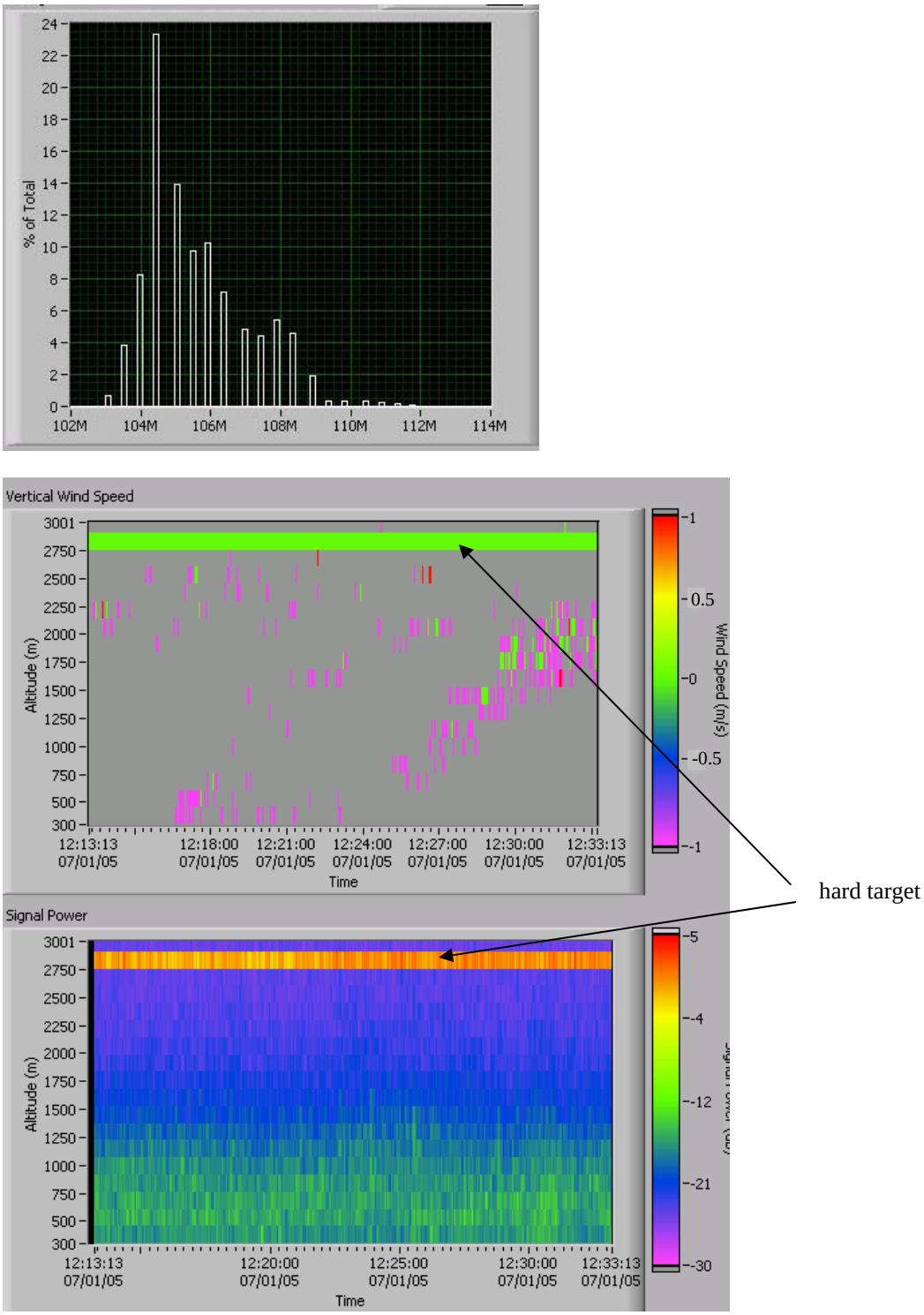

Figure 8: Assessment of the effects of laser frequency jitter. The upper plot is a histogram of the measured beat frequency between the outgoing laser pulse and local oscillator. The lower plot shows the results of striking a hard target at 2.8 km range using the same data set described by the histogram. Measured speed of the hard target consistently reads 0 m/s, indicating the frequency jitter has been corrected.

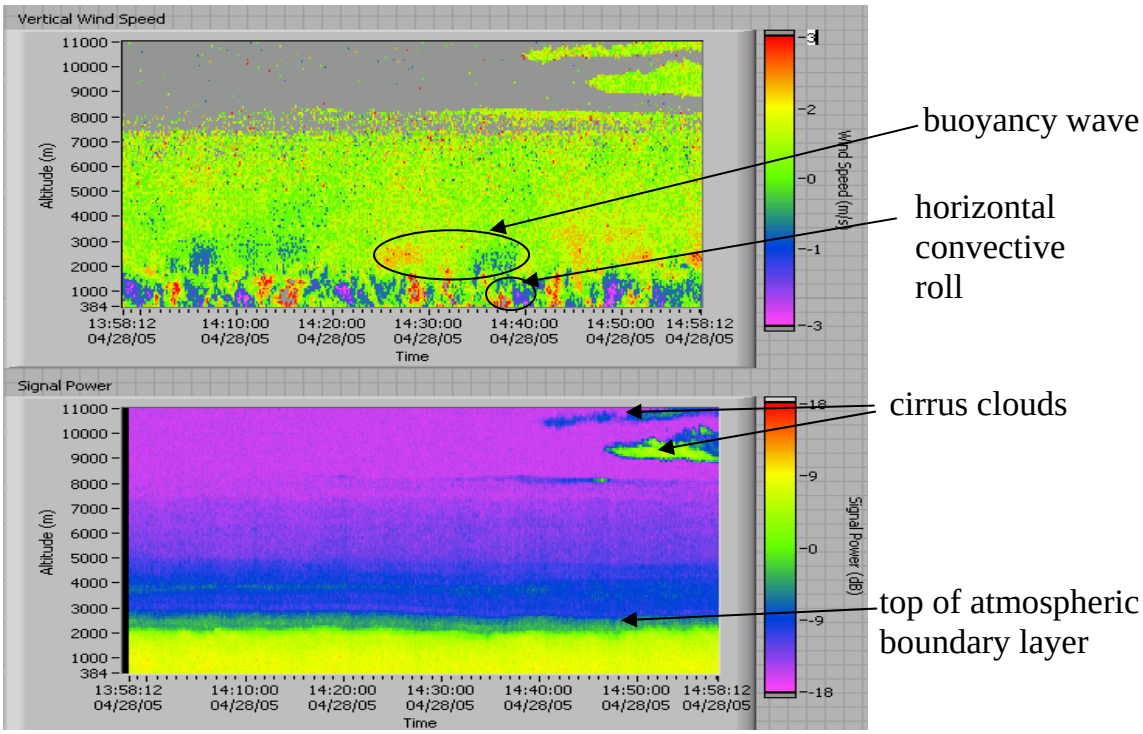

Figure 9: Profile of vertical wind. The upper plot shows wind speed with red being updraft and purple being downdraft, and the lower plot shows backscatter signal power. No $1/R^2$ correction has been made in the signal power.

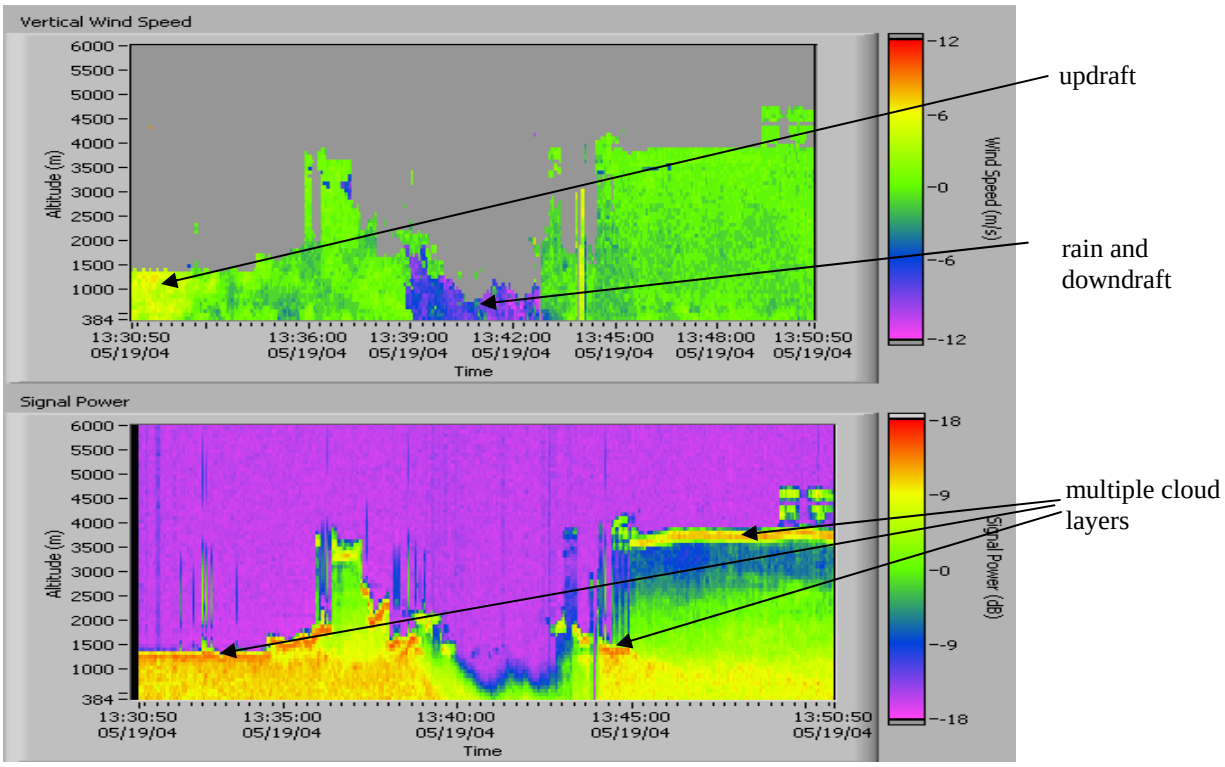

Figure 10: Profile of vertical wind during a thunderstorm. The upper plot shows wind speed with red being updraft and purple being downdraft, and the lower plot shows backscatter signal power. No $1/R^2$ correction has been made in the signal power.

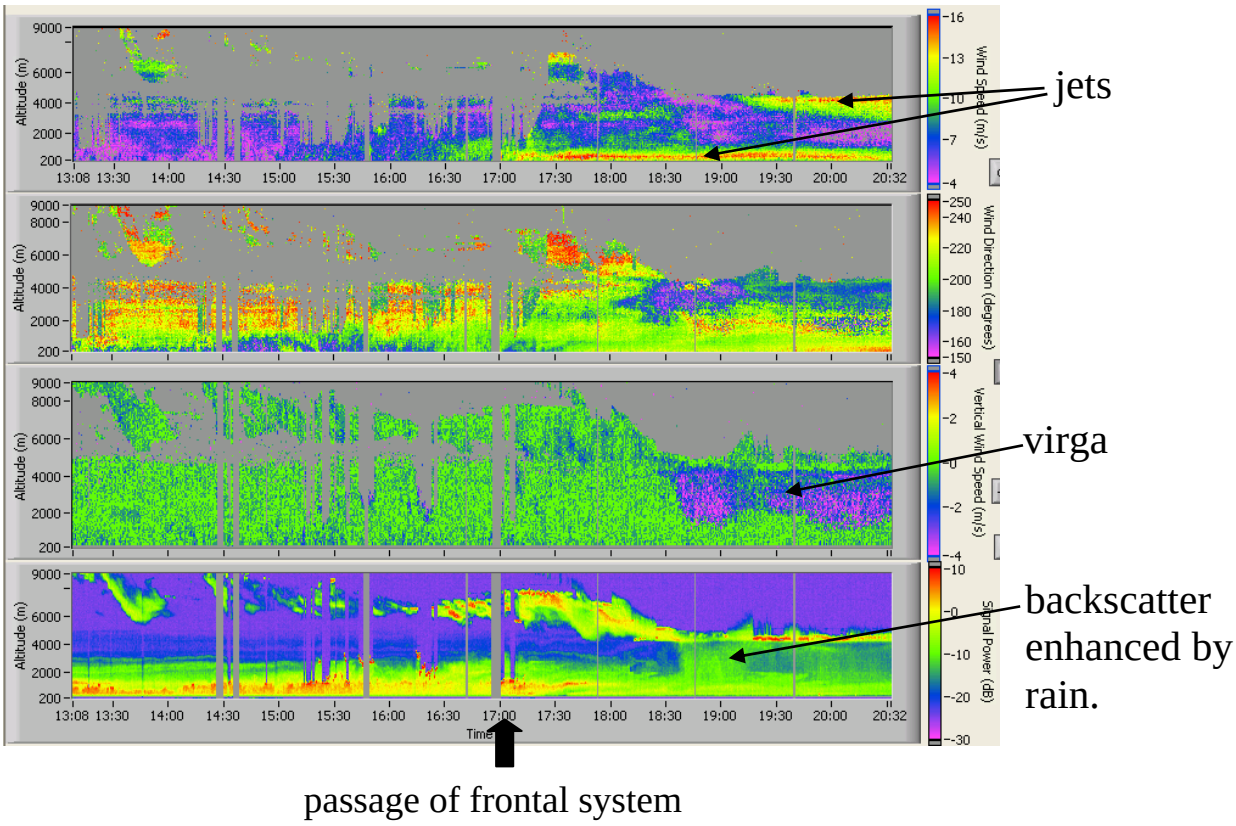

Figure 11: Wind profile taken on June 28, 2005. A weather front passed through in the middle of the data set. The panels of data show, from top to bottom, 1) horizontal wind speed, 2) horizontal wind direction, 3) vertical wind speed (red upward, purple downward), and 4) backscatter signal power from zenith viewing. Gaps occur in the data as one set of data ends and the other begins or as problems occurred with the control computer. A speed or direction display in gray indicates that the measured value is out of range of the color scale

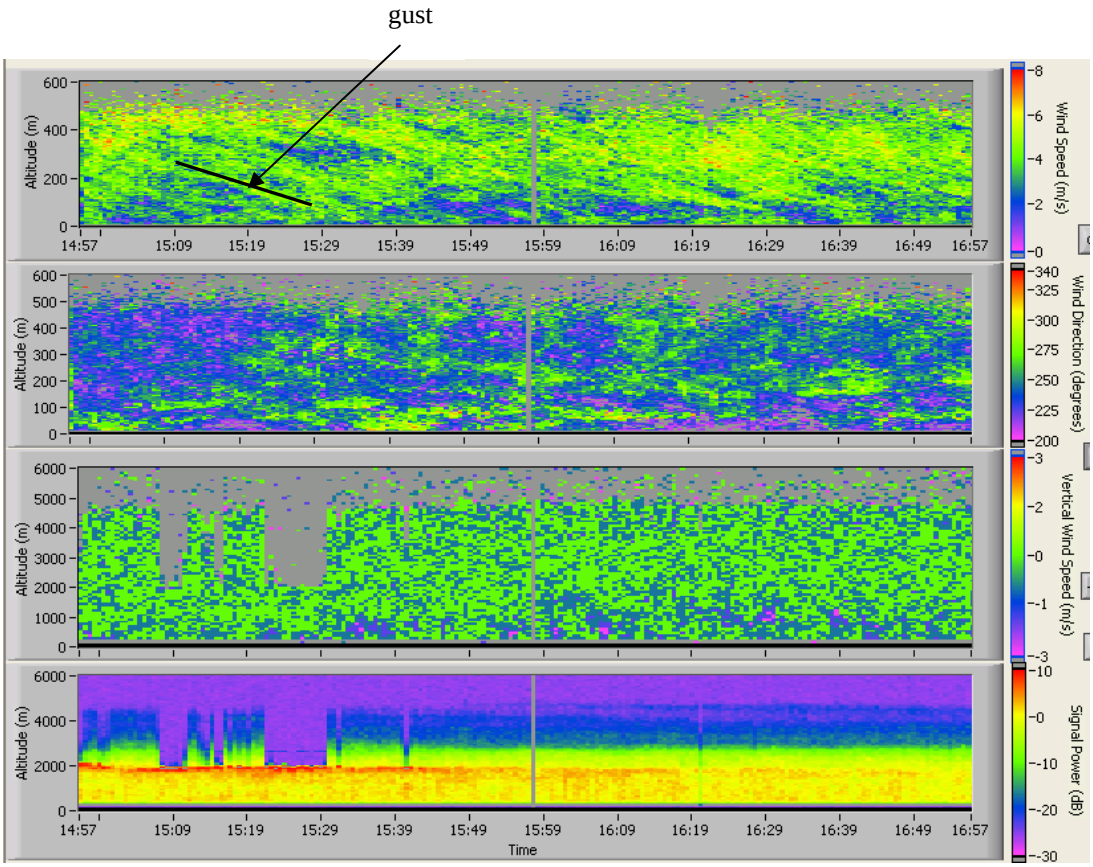

Figure 12: Low altitude wind profile taken on July 25, 2005. The panels of data show, from top to bottom, 1) horizontal wind speed, 2) horizontal wind direction, 3) vertical wind speed (red upward, purple downward), and 4) backscatter signal power from zenith viewing. Gaps occur in the data as one set of data ends and the other begins or as problems occurred with the control computer. A speed or direction display in gray indicates that the measured value is out of range of the color scale.

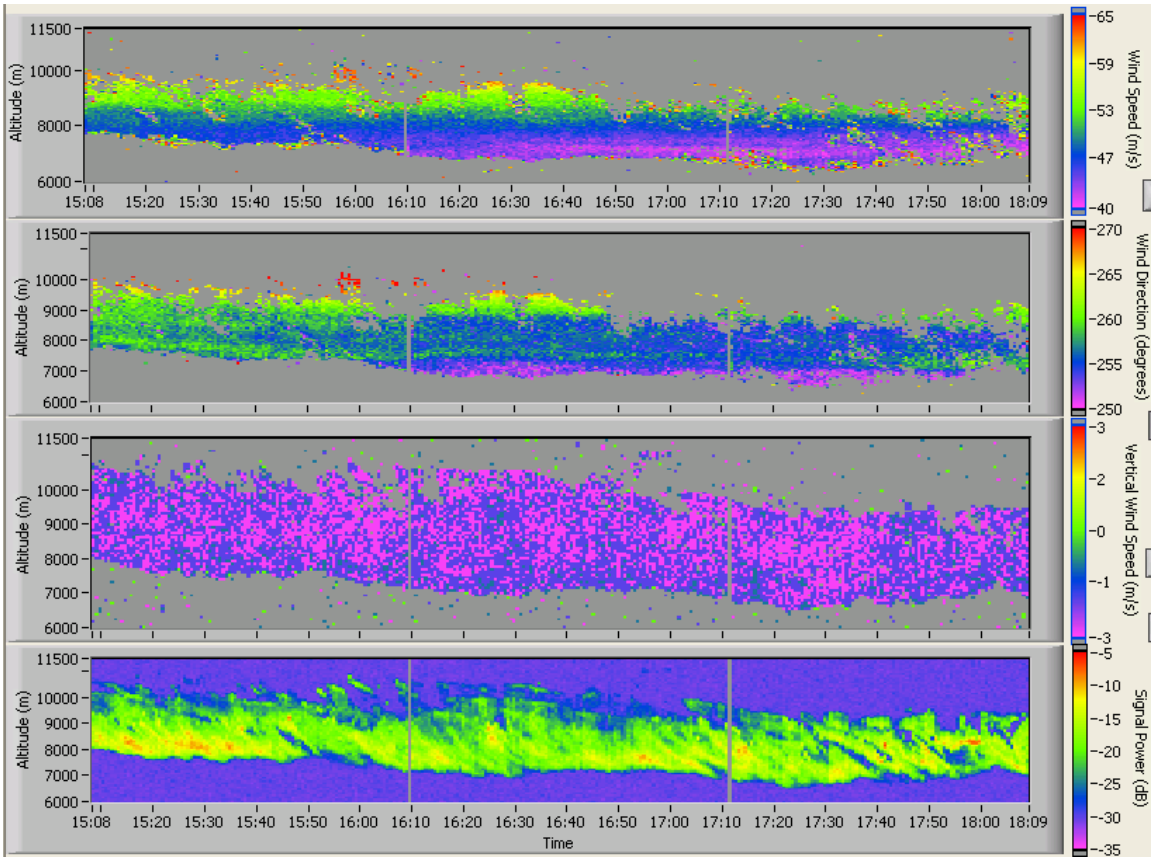

Figure 13: Cirrus cloud probed by lidar on December 16, 2005. High wind speeds are involved with this cloud inside the jet stream. The panels of data show, from top to bottom, 1) horizontal wind speed, 2) horizontal wind direction, 3) vertical wind speed (red upward, purple downward), and 4) backscatter signal power from zenith viewing. Gaps occur in the data as one set of data ends and the other begins or as problems occurred with the control computer. A speed or direction display in gray indicates that the measured value is out of range of the color scale